This article may be downloaded for personal use only. Any other use requires prior permission of the author and AIP Publishing. This article appeared in: Langfeldt, F. and W. Gleine. Optimizing the bandwidth of plate-type acoustic metamaterials. *The Journal of the Acoustical Society of America* 148(3) (2020): 1304–1314 and may be found at https://doi.org/10.1121/10.0001925.

Optimizing the bandwidth of plate-type acoustic metamaterials

Felix Langfeldt[1] and Wolfgang Gleine[1]

Department of Automotive and Aeronautical Engineering,

Hamburg University of Applied Sciences, Berliner Tor 7a, D–20099 Hamburg, Germany[a)]

Accepted Manuscript

Plate-type acoustic metamaterials (PAM) consist of a thin film with multiple periodically attached masses. Although these metamaterials can be very lightweight and thin, the resulting sound transmission loss at low frequencies can be much larger than the corresponding mass-law. This is a result of anti-resonances at which the sound transmission through the PAM is strongly reduced. One general challenge, however, is that the anti-resonances are only very narrowband. This makes the application of PAM to noise control problems with broadband noise sources or changing tonal sources difficult. In this contribution different design strategies to improve the bandwidth of PAM for low-frequency noise control applications (multiple masses per unit cell or stacking multiple PAM layers) are evaluated using optimizations. An efficient modal based model is employed to represent the PAM using their eigenfrequencies and modal masses. The model is validated using simulations and experimental measurements. The optimization results show that it is possible to significantly improve the bandwidth of PAM using the investigated design strategies. In fact, it is shown that the same bandwidths can be achieved either using multiple masses or multiple PAM layers. This allows for some flexibility in the design of suitable noise control treatments with PAM.

Accepted Manuscript

[a]; Felix.Langfeldt@haw-hamburg.de

I. INTRODUCTION

Locally resonant sonic materials consist of periodically arranged resonant unit cells and can strongly reduce the transmission of sound waves at unit cell sizes much smaller than the wavelength (Ma and Sheng, 2016). In these types of acoustic metamaterials, the band-gaps with high sound transmission loss are related to destructive interference effects caused by the resonances of the unit cells. However, since the physical mechanism of locally resonant sonic materials is linked to resonances, their bandwidth typically is very narrowband.

There exists a wide range of realizations of locally resonant sonic materials with many different properties (Huang *et al.*, 2016; Ma and Sheng, 2016; Zangeneh-Nejad and Fleury, 2019). The so-called plate-type acoustic metamaterials (PAM) are particularly promising for applications demanding lightweight low-frequency noise treatments. PAM are based on investigations by Kurtze (1959) and consist of a thin film with rigid masses periodically attached to it. The locally resonant behavior of PAM originates from the added masses in each unit cell and the film material around the masses, which acts as an elastic spring. At low frequencies, PAM can exhibit acoustic anti-resonances at which the sound transmission loss (STL) can be much greater than that of a homogeneous film with equal mass. At these anti-resonance frequencies the masses and the surrounding thin film vibrate out of phase in such a manner that the surface-averaged displacement amplitude is near zero and the sound radiation is greatly diminished due to the sub-wavelength size of the unit cells (Yang *et al.*, 2010). For example, this behavior can be exploited to improve the sound reduction properties of glass wool insulation at low frequencies (Langfeldt and Gleine, 2019a). However, due

Accepted Manuscript

to the resonant behavior of the unit cells, this improvement is only limited to a narrow frequency band. The effect of random deviations from the idealized periodic structure of PAM (for example due to manufacturing inaccuracies) was investigated by Langfeldt and Gleine (2020). It was found that only very large deviations can have a significant impact on the sound transmission loss performance of PAM. However, this primarily results in a reduced STL improvement at the anti-resonances and not so much in an improved bandwidth.

Improving the bandwidth of similar acoustic metamaterials was already subject of study in the literature. Yang *et al.* (2010) demonstrated that stacking multiple layers of membrane-type acoustic metamaterials (MAM) with different tunings can lead to high STL values over a broad frequency range below 1 kHz. Another way for increasing the bandwidth of such metamaterials is to use multiple masses in one unit cell (Leblanc and Lavie, 2017; Lu *et al.*, 2020; Mei *et al.*, 2012). Further bandwidth improvements have been shown to be possible by using perforations in the added masses (Langfeldt *et al.*, 2017) or the cavities between bilayer MAM (Ang *et al.*, 2018). Thus, in principle it is well understood by what design strategies the bandwidth of PAM could possibly improved. However, most of the current literature on this topic does not take into account important constraints such as the overall mass or thickness of the metamaterials. Also, it is not clear what strategy is more effective for improving the bandwidth of PAM—for example, is it better to increase the number of masses per unit cell or the number of layers?

The focus of this contribution is to systematically evaluate the bandwidth improvement of PAM with multiple masses per unit cell as well as multi-layered PAM, as compared to a single PAM layer with one mass per unit cell at the same overall surface mass density.

Accepted Manuscript

For this purpose, an efficient optimization method is employed to identify the best possible design to achieve higher bandwidths in a given frequency range. The efficient PAM model used in the optimizations is described and validated using numerical and experimental data in section II. The optimization results for single- and multi-layered PAM are presented and discussed in section III. Finally, the conclusions of this investigation are summarized in section IV.

II. EFFICIENT MODELING OF PLATE-TYPE ACOUSTIC METAMATERIALS

In this section, an efficient methodology for modeling the sound transmission properties of plate-type acoustic metamaterials with periodic unit cells and unconstrained unit cell edges (like the metamaterials investigated in (Kurtze, 1959; Langfeldt and Gleine, 2019a, 2020)) will be presented. This model will be employed in the optimizations of different PAM designs. First, the modal based method for efficiently obtaining the effective surface mass density of PAM is introduced. In section II B it is explained how the sound transmission loss of single layer and multi-layered PAM is calculated from the effective surface mass density. Since the modal based model in section II A only considers a single PAM layer, the transfer matrix method will be employed in section II B to obtain the transmission loss of structures consisting of multiple PAM layers. This methodology is validated in section II C using finite element model simulations and sound transmission loss measurement data.

Accepted Manuscript

A. Modal based effective surface mass density calculation

Since many different unit cell designs of the PAM are to be investigated in the optimizations, an efficient numerical method for estimating the bandwidth of a PAM design is required. In this work, a modal method based on the homogenization theory given by Yang *et al.* (2014) will be employed to estimate the frequency-dependent effective surface mass density m''_{eff} of the metamaterial. From (Yang *et al.*, 2014) it follows that m''_{eff} can be expressed in terms of the angular eigenfrequencies $\omega_i = 2\pi f_i$ and mode shapes $\mathbf{u}_i$ of the unit cell as

$$m''_{\text{eff}} = -m''_0 \left(\sum_{i=0}^{m} \frac{1}{\mu_i} \frac{\omega^2}{\omega_i^2 - \omega^2} \right)^{-1}, \tag{1}$$

where m''_0 is the static surface mass density of the PAM and i corresponds to the mode index of the PAM. The normalized modal masses μ_i are given by

$$\mu_i = \frac{1}{m''_0 S} \frac{\int_\Omega \rho {\mathbf{u}_i}^H \mathbf{u}_i \mathrm{d}\Omega}{|\langle W_i \rangle|^2}. \tag{2}$$

In Equation 2, Ω denotes the domain of the unit cell (film and masses), ρ is the density of the film and mass material, $\mathbf{u}_i$ is the modal displacement vector field, ${\mathbf{u}_i}^H$ is the Hermitian transpose of $\mathbf{u}_i$, and S is the unit cell area. $\langle W_i \rangle$ represents the surface-averaged value of the surface-normal mode shape component W_i along S. It should be noted that the unit cell edges of PAM are not constrained. Therefore, the 0-th mode of each PAM unit cell is a rigid body mode with $\omega_0 = 0\,\mathrm{rad\,s^{-1}}$ and uniform displacement, leading to $\mu_0 = 1$. Taking this into account and furthermore introducing damping via a mechanical loss factor η of the

Accepted Manuscript

PAM, Equation 1 can be reformulated as follows:

$$m''_{\text{eff}} = m''_0 \left(1 - \sum_{i=1}^{m} \frac{1}{\mu_i} \frac{\omega^2}{\omega_i^2 (1 + \mathrm{i}\eta) - \omega^2} \right)^{-1}. \tag{3}$$

From this it follows that for $\omega \to 0$ the effective surface mass density approaches the static surface mass density m''_0 of the PAM.

B. Sound transmission loss calculation

For a single PAM, the effective surface mass density in Equation 3 can be used to calculate the normal incidence sound transmission loss TL by using the mass-law formula

$$\mathrm{TL} = 20 \lg \left| 1 + \frac{\mathrm{i}\omega m''_{\text{eff}}}{2 Z_0} \right|, \tag{4}$$

where $Z_0 = \rho_0 c_0$ is the characteristic impedance of the fluid. For a multi-layered stack of PAM the transmission loss can be calculated using the transfer matrix $\mathbf{T}$ of the stack, given by

$$\mathbf{T} = \begin{bmatrix} T_{11} & T_{12} \\ T_{21} & T_{22} \end{bmatrix} = \mathbf{T}_1^{(\text{PAM})} \cdot \prod_{j=2}^{n} \left(\mathbf{T}_{j-1,j}^{(\text{Air})} \cdot \mathbf{T}_j^{(\text{PAM})} \right), \tag{5}$$

where

$$\mathbf{T}_j^{(\text{PAM})} = \begin{bmatrix} 1 & \mathrm{i}\omega m''_{\text{eff},j} \\ 0 & 1 \end{bmatrix} \tag{6}$$

and

$$\mathbf{T}_{j-1,j}^{(\text{Air})} = \begin{bmatrix} \cos(k_0 d_{j-1,j}) & \frac{\mathrm{i}\omega\rho_0}{k_0} \sin(k_0 d_{j-1,j}) \\ \frac{-k_0}{\mathrm{i}\omega\rho_0} \sin(k_0 d_{j-1,j}) & \cos(k_0 d_{j-1,j}) \end{bmatrix} \tag{7}$$

Accepted Manuscript

are the transfer matrices of the j-th PAM layer with the effective surface mass density $m''_{\mathrm{eff},j}$ and of the air layer between the layers $j-1$ and j with the wave number $k_0 = \omega/c_0$ and the air layer thickness $d_{j-1,j}$, respectively (Allard and Atalla, 2009). The transmission loss of the multi-layered structure can be calculated from the elements of $\mathbf{T}$ given in Equation 5 via

$$\mathrm{TL} = 20\lg\left(\frac{1}{2}\left|T_{11} + \frac{T_{12}}{Z_0} + Z_0 T_{21} + T_{22}\right|\right). \tag{8}$$

C. Validation of the PAM model

1. *Finite element simulations*

The accuracy of the simplified expressions given in section II A and section II B is evaluated with numerical simulations of PAM unit cells using the finite element method (FEM). Two mass configurations are considered in the validation: The unit cell geometry of a PAM with two semi-circular masses is shown in Figure 1 and Figure 2 illustrates the setup for a PAM unit cell with a single circular mass in the center. The film material is specified as polycarbonate (density $\rho = 1310\,\mathrm{kg\,m^{-3}}$, Young's modulus $E = 2.3\,\mathrm{GPa}$, Poisson's ratio $\nu = 0.4$, structural loss factor $\eta = 5\,\%$) with a film thickness of $h_\mathrm{F} = 25\,\mathrm{\mu m}$. The masses are made of steel ($\rho = 7860\,\mathrm{kg\,m^{-3}}$, $E = 207\,\mathrm{GPa}$, $\nu = 0.3$) and in the semi-circular mass case each mass weighs $M = 11.9\,\mathrm{mg}$, while in the circular mass case $M = 9.8\,\mathrm{mg}$. This results in the static surface mass densities $m''_0 = 0.5\,\mathrm{kg\,m^{-2}}$ for the double mass unit cell and $m''_0 = 0.22\,\mathrm{kg\,m^{-2}}$ for the single mass PAM. The discretization of the two unit cell designs is

Accepted Manuscript

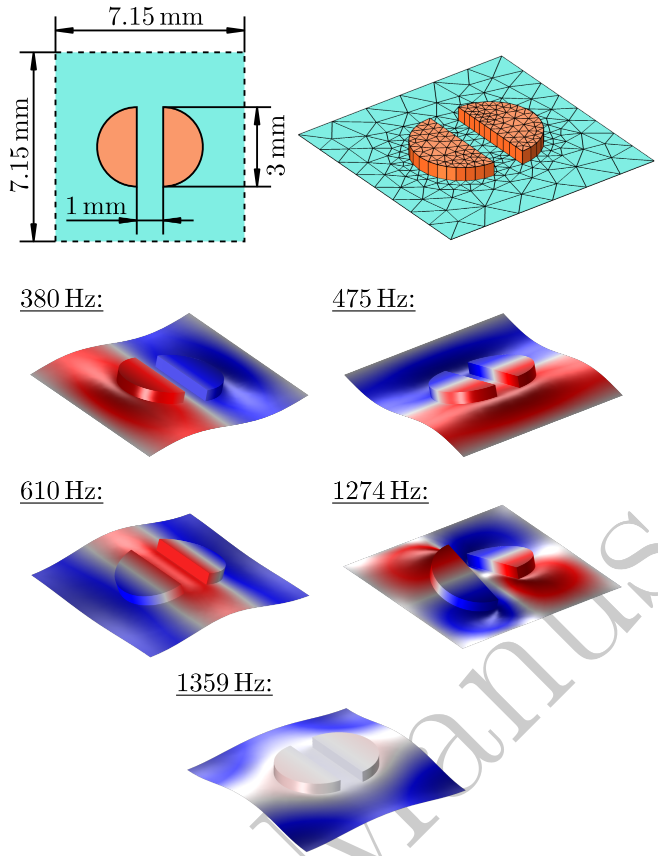

FIG. 1. (Color online) Unit cell geometry, mesh, and mode shapes of the PAM unit cell with two semi-circular masses considered in the validation of the PAM model.

shown in Figure 1 and Figure 2. Periodic boundary conditions are prescribed at the edges of the unit cells to represent the behavior of an infinitely extending metamaterial.

First, an eigenvalue analysis of the two unit cells is performed to obtain the resonance frequencies below 2 kHz and the associated mode shapes to be used in Equation 3 for calculating m''_{eff} of the two different PAM. The simulated mode shapes are shown in the bottom of Figure 1 and Figure 2. Table I and Table II provide a more detailed overview of the computed eigenmodes and the resulting normalized modal masses μ_i. These values are then used to calculate the normal incidence TL of the two PAM using Equation 3 and Equation 4.

Accepted Manuscript

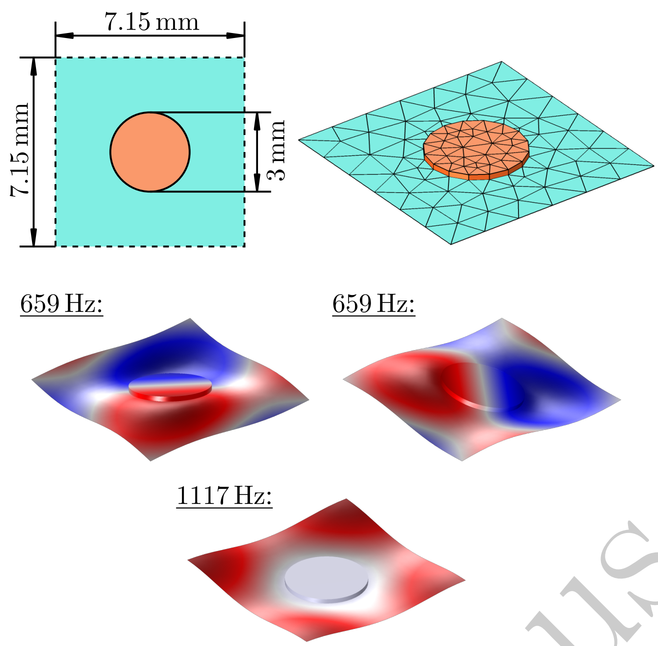

FIG. 2. (Color online) Unit cell geometry, mesh, and mode shapes of the PAM unit cell with one circular mass considered in the validation of the PAM model.

Accepted Manuscript

TABLE I. Modal parameters for the PAM unit cell shown in Figure 1.

i	f_i	$\lvert\langle W_i\rangle\rvert^2$	μ_i
1	380	5.94×10^{-11}	1.73×10^{5}
2	475	1.48×10^{-13}	3.12×10^{7}
3	610	1.81×10^{-6}	1.24
4	1274	7.49×10^{-10}	3.59×10^{3}
5	1359	1.08×10^{-5}	0.165
	Hz	m^2	—

TABLE II. Modal parameters for the PAM unit cell shown in Figure 2.

i	f_i	$\|\langle W_i \rangle\|^2$	μ_i
1	659	1.89×10^{-10}	2.67×10^4
2	659	1.85×10^{-11}	2.77×10^5
3	1117	1.08×10^{-5}	0.315
	Hz	m^2	—

For the first unit cell, the number of eigenmodes considered in the calculations is $m = 5$. In case of the single mass unit cell, m equals to 3.

An overview of the model for obtaining the TL of the PAM using fully coupled vibro-acoustic FEM simulations is shown in Figure 3(a). Two fluid domains are coupled to the top and bottom sides of the PAM. The fluid domains are truncated using non-reflecting boundaries and the lateral boundaries are specified as periodic boundaries, just like the edges of the PAM unit cell. The PAM is excited by an incoming plane acoustic wave and the resulting TL is evaluated using the sound power transmitted through the PAM.

Figure 3(b) shows a comparison of the TL results from the modal based effective surface mass density calculations (curves) and fully coupled vibro-acoustic FEM simulations (symbols). The solid curves and circles represent the results for the PAM unit cell with two masses (Figure 1), the dashed curves and squares correspond to the unit cell with only one mass (Figure 2). In general, the agreement with the fully coupled simulation results is very good. This indicates that the modal based formulation of the effective surface mass

Accepted Manuscript

density of PAM is an efficient yet accurate enough way for predicting the noise reduction performance of PAM. It should be noted that in the transmission loss curves in Figure 3(b) only some of the PAM resonances given in Table I and Table II appear as dips. In case of the PAM with two masses, for example, only two dips at $f_3 = 610\,\mathrm{Hz}$ and $f_5 = 1359\,\mathrm{Hz}$ can be seen. The other resonance frequencies do not appear, because these modes have anti-symmetric mode shapes, the surface averaged film displacements $\langle W_i \rangle$ are close to zero, and, consequently, the normalized modal masses μ_i are very high. Therefore, these modes do not couple with the incident sound waves and can therefore be neglected when considering the transmission of sound through the PAM.

The TL of these two PAM unit cells stacked on top of each other with a spacing of $d_{1,2} = 5\,\mathrm{mm}$ is shown in Figure 4(a). Again, a very good agreement between the modal based transfer matrix model (TMM) and the fully coupled FEM can be observed. The TMM therefore is well-suited to predict the transmission loss of stacked PAM arrangements, even for small layer spacings. The results in Figure 4(a) also indicate that the anti-resonances of the PAM are retained in the multi-layered arrangement, which can be potentially exploited for bandwidth improvements. The resonance dips, on the other hand, are not necessarily the same as for the individual PAM: In the multi-layered case, the TL dips occur in between the anti-resonances, roughly at the same frequencies at which the TL curves of the individual PAM layers shown in Figure 3(b) intersect.

To investigate the influence of the layer spacing, Figure 4(b) shows a more detailed view of the three anti-resonances of the multi-layered PAM for three different spacings $d_{1,2} = 1$, 2, and 5 mm. In both the FEM and TMM results the impact of the layer spacing is negligibly

Accepted Manuscript

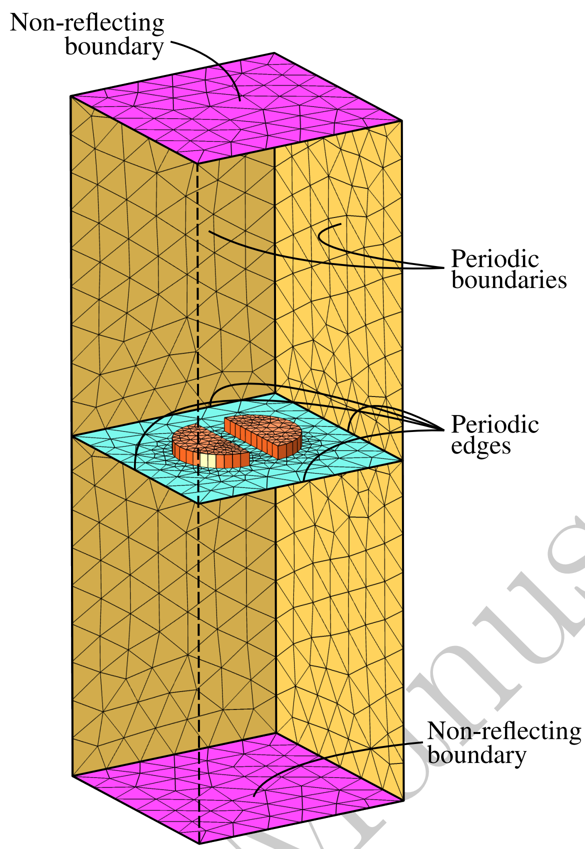

(a)

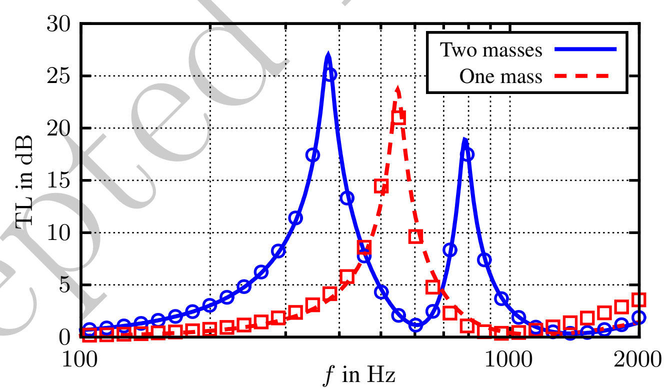

(b)

FIG. 3. (Color online) Normal incidence sound transmission loss TL of different single layer PAM configurations. (a) General overview of the finite element model; (b) TL values obtained from the modal based effective surface mass density model (curves) and fully coupled FEM simulations (symbols).

Accepted Manuscript

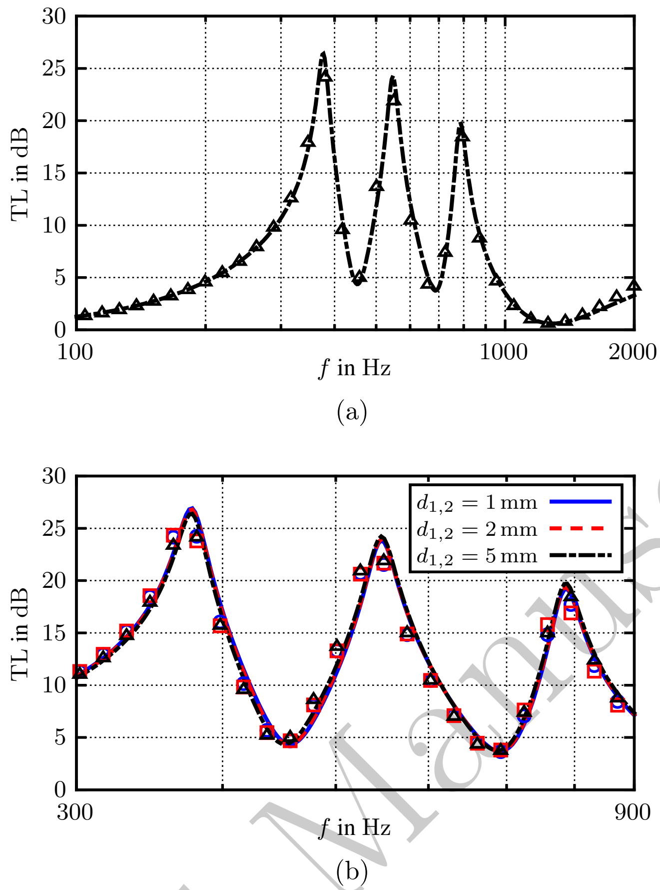

FIG. 4. (Color online) Normal incidence sound transmission loss TL of a two layer PAM consisting of the two unit cells shown in Figure 1 and Figure 2. The curves indicate results obtained from the modal based effective surface mass density model and symbols represent FEM results. (a) PAM layer spacing $d_{1,2} = 5\,\mathrm{mm}$; (b) Detailed view of the transmission loss for different PAM layer spacings.

small. In fact, from Equation 7 it can be deduced that for spacings $d_{j-1,j}$ much smaller than the acoustic wavelength $k_0 d_{j-1,j} \ll 1$ and Equation 7 can be approximated as

$$\mathbf{T}_{j-1,j}^{(\mathrm{Air})} \approx \begin{bmatrix} 1 & \mathrm{i}\omega\rho_0 d_{j-1,j} \\ 0 & 1. \end{bmatrix} \tag{9}$$

Accepted Manuscript

This means that thin air layers between multiple PAM layers act like incompressible fluid volumes with surface mass densities of $\rho_0 d_{j-1,j}$. Since the density of air is typically much smaller than the (effective) density of the PAM, the contribution of the air layers to the total sound transmission behavior of multi-layered PAM is negligible, as long as $k_0 d_{j-1,j} \ll 1$. This explains the very small impact of the layer spacing in Figure 4(b).

2. *Transmission loss measurements*

In order to validate the modal based PAM model for a more realistic setup of a finite sized PAM under diffuse field excitation, the results of the PAM model are compared to sound transmission loss measurement data. For this purpose, the measurement results of the PAM sample from Langfeldt and Gleine (2020) are used. Figure 5(a) shows a photograph of the PAM mounted inside a transmission loss test window between a reverberation chamber and a hemi-anechoic chamber. The $1\,\mathrm{m} \times 1.2\,\mathrm{m}$ large sample consists of a $h_\mathrm{F} = 0.75\,\mathrm{mm}$ thick polycarbonate film and 180 cylindrical steel masses, each with a diameter of 30 mm and weight $M = 5.8\,\mathrm{g}$, aligned in a square lattice with a spacing of 77.5 mm. The resulting overall surface mass density of the PAM is given by $m_0'' = 1.9\,\mathrm{kg\,m^{-2}}$. The perimeter of the sample was fixed at the frame of the transmission window. Further details about the measured PAM sample and the sound transmission loss measurement method can be found in (Langfeldt and Gleine, 2020).

In the modal based model, the PAM is represented by the first non-zero symmetric mode (i.e. $m = 1$) with $f_1 = 299\,\mathrm{Hz}$ and an associated normalized modal mass of $\mu_1 = 2.43$. These values have been obtained from a numerical modal analysis using a FEM model

Accepted Manuscript

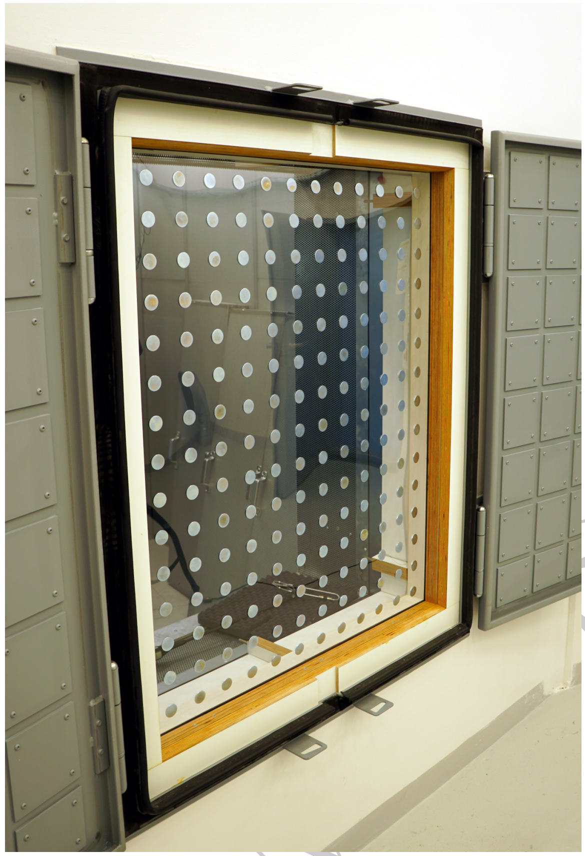

(a)

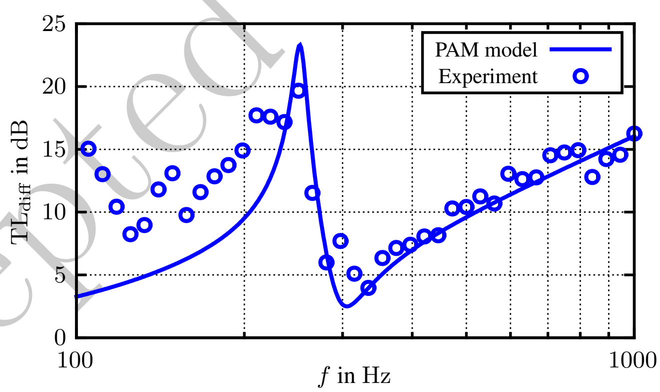

(b)

FIG. 5. (Color online) Diffuse incidence sound transmission loss $\mathrm{TL_{diff}}$ of the experimental PAM test sample measured in (Langfeldt and Gleine, 2020). (a) Photograph of the PAM test sample mounted inside the transmission loss test suite; (b) Comparison of the measurement and PAM model results.

of the unit cell of the PAM, similar to the method used in section II C 1. Damping was taken into account in Equation 3 using the structural loss factor of polycarbonate $\eta = 5\,\%$. Since the measured STL of the PAM was obtained under diffuse field incidence, the diffuse transmission loss was estimated from the effective surface mass density of the PAM using the formula

$$\mathrm{TL}_{\mathrm{diff}} = -10\lg\left(\frac{\int\limits_0^{\theta_{\max}} \tau_\theta \sin(\theta)\cos(\theta)\,\mathrm{d}\theta}{\int\limits_0^{\theta_{\max}} \sin(\theta)\cos(\theta)\,\mathrm{d}\theta}\right) \tag{10}$$

with the transmission coefficient at the plane wave incidence angle θ (Bies and Hansen, 2009)

$$\tau_\theta = \left|1 + \frac{\mathrm{i}\omega m''_{\mathrm{eff}}\cos\theta}{2Z_0}\right|^{-2}. \tag{11}$$

The limiting angle $\theta_{\max}$ for the given laboratory setup has been estimated in a previous experiment as $\theta_{\max} = 72°$ (Langfeldt *et al.*, 2020).

Figure 5(b) shows a comparison of the measurement results (symbols) and the analytical results using the modal based PAM model (curve). Generally, the agreement between the data is good. Only at frequencies below the anti-resonance frequency of the PAM the PAM model results underestimate the experimental STL. A possible explanation for this is presumed to be the reduced diffuseness of the sound field in the reverberation chamber at low frequencies. Also, the spatial windowing effect due to the finite sized sample (Fahy and Gardonio, 2007) can be an explanation for the larger measured STL compared to the STL predicted by the PAM model which does not take this effect into account. A comparison of the experimental data with FEM simulation results of a finite sized PAM sample, just as in the experiments, by Langfeldt and Gleine (2020)—which shows a better agreement at

Accepted Manuscript

very low frequencies—indicates that the latter is the main reason for the higher STL values below the first anti-resonance frequency in the experiments, as compared to the analytical model. Nevertheless, the anti-resonance as well as the STL dip at the subsequent resonance around $f_1 = 299\,\mathrm{Hz}$ is represented very well by the PAM model, even in the case of a more realistic setup (diffuse incidence and finite sized sample) and taking into account only the first non-zero symmetric PAM unit cell mode. Although the anti-symmetric modes in principle couple with the obliquely incident waves that are present in a diffuse sound field, this coupling is very weak and can therefore be neglected, as evident by the good agreement in Figure 5(b). The main reason for the weak coupling with anti-symmetric modes is the small size of the unit cells (compared to the wavelength) resulting in a virtually uniform sound pressure field exciting each unit cell (Langfeldt and Gleine, 2019b). Furthermore, it should be emphasized that although the PAM model delivers results for an infinite metamaterial, the main characteristics of the experimental PAM sample (which is finite sized and subject to fixed boundary conditions at the perimeter) are adequately captured by this idealization. This indicates that the modal based model, despite its simple formulation and computational efficiency, is accurate enough to systematically investigate the bandwidth optimization of PAM.

III. PAM DESIGNS WITH IMPROVED BANDWIDTH

In this section, the optimized modal PAM unit cell parameters to achieve a maximized transmission loss improvement bandwidth will be presented and discussed. This bandwidth is defined herein as the percentage within a given frequency interval $f \in [f_{\min}, f_{\max}]$ for

Accepted Manuscript

which the STL of the metamaterial exceeds the mass-law transmission loss $\mathrm{TL}_{\mathrm{mass}}$ by at least 6 dB. Numerically, this quantity can be evaluated using the expression

$$\mathrm{BW} = \frac{1}{f_{\max} - f_{\min}} \int_{f_{\min}}^{f_{\max}} \sigma(f)\,\mathrm{d}f \tag{12}$$

where

$$\sigma(f) = \begin{cases} 1 & \text{if} \quad \mathrm{TL}(f) - \mathrm{TL}_{\mathrm{mass}}(f) \geq 6\,\mathrm{dB} \\ 0 & \text{else} \end{cases}. \tag{13}$$

Thus, a bandwidth of $\mathrm{BW} = 100\,\%$ means that the mass-law is exceeded by at least 6 dB within the whole frequency range of interest. A value of 0 % indicates, on the other hand, that this target is not achieved at any frequency between $f_{\min}$ and $f_{\max}$. At this point it should be emphasized that the definition of bandwidth used in this contribution is only one of many different ways to define the bandwidth of a metamaterial. A suitable definition is highly problem dependent—for example, using other measures like the half power bandwidth might be appropriate in certain noise control applications. The authors have chosen the bandwidth definition using Equation 12, because a STL improvement by 6 dB is a notable improvement in noise reduction. Also, the decrease in STL at higher frequencies due to the decoupling of the masses from the surrounding film is not taken into account because at these frequencies conventional noise control measures such as fibrous materials become quite efficient and can be used in conjunction with the PAM (Langfeldt and Gleine, 2019a).

The present section is divided into five sub-sections: First, the optimal modal properties of a PAM with a single mass are investigated systematically in section III A. The optimization method which is employed to identify the optimized properties of PAM configurations with multiple masses or multiple PAM layers is described in section III B. Section III C regards

Accepted Manuscript

the results obtained for a single PAM layer with multiple masses in one unit cell. Then, section III D discusses the optimized bandwidth for stacked PAM layers with each layer having only a single mass per unit cell. The results are compared to an optimized single PAM layer with one mass, as obtained in section III A. Finally, in section III E it is shown how the bandwidth is affected for PAM with combinations of multiple layers and multiple masses.

In all cases, the total surface mass density is the same with $m''_0 = 0.5\,\mathrm{kg\,m^{-2}}$. A structural loss factor of $\eta = 5\,\%$ is specified and the frequency range considered for evaluating the bandwidth according to Equation 12 is between $f_{\mathrm{min}} = 100\,\mathrm{Hz}$ and $f_{\mathrm{max}} = 400\,\mathrm{Hz}$. All results presented in this section have been obtained using the efficient PAM model presented in section II.

A. Unit cell with a single mass

As shown in section II C, the STL at the first anti-resonance of a PAM with a single mass per unit cell is very well represented using only the first non-zero symmetric mode (i.e. $m = 1$) of the unit cell. Furthermore, assuming that m''_0 and η are prescribed by design constraints and material selections, it follows from Equation 3 that this leaves the modal parameters f_1 and μ_1 of the first mode as the only free parameters. Thus, the bandwidth of this most simple PAM design can be optimized by exploring the full parameter space of f_1 and μ_1. This aids in understanding what the STL spectrum of a PAM with optimized bandwidth BW, in the sense of the definition given in Equation 12, should look like. Furthermore, these

Accepted Manuscript

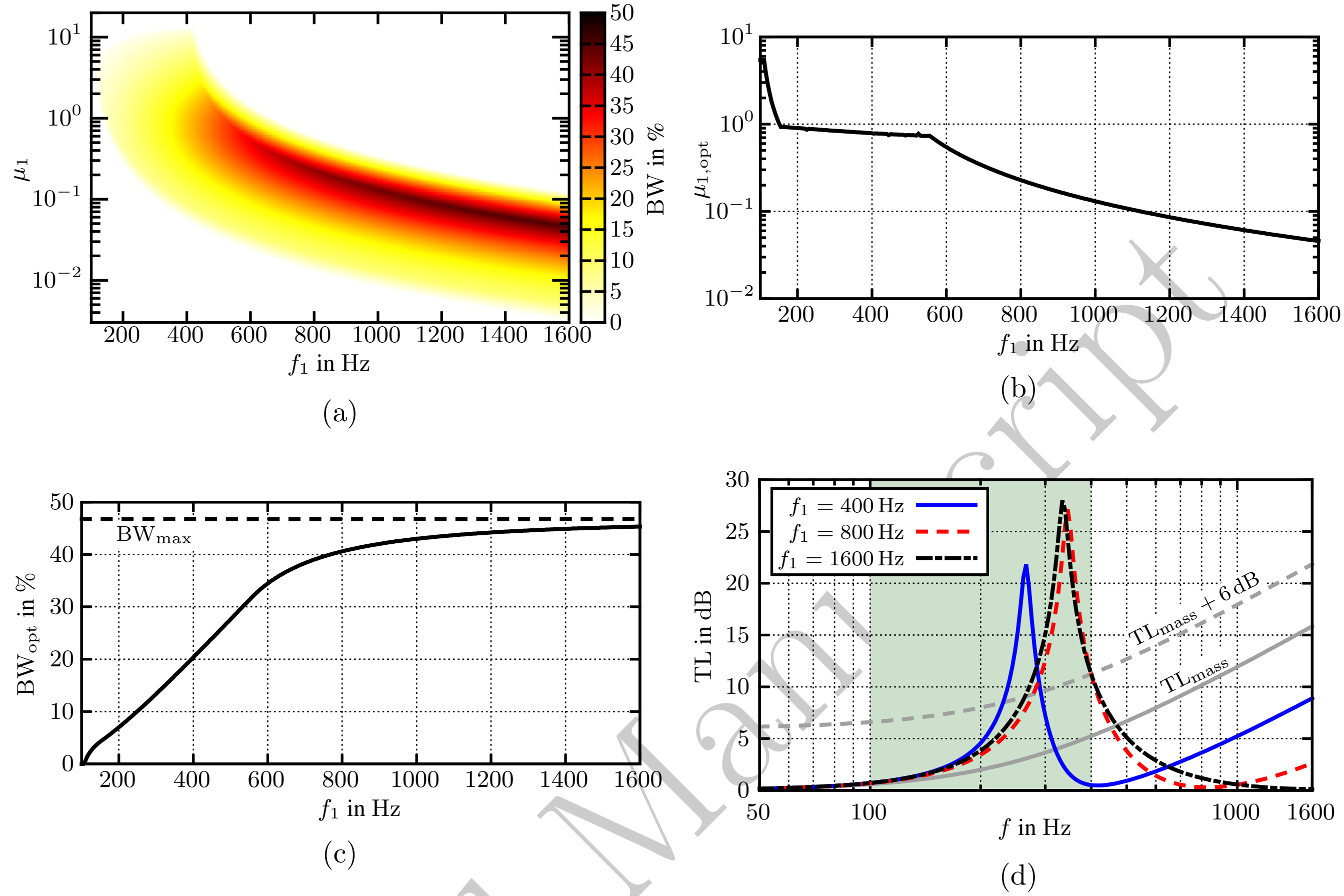

FIG. 6. (Color online) Optimization of the resonance frequency f_1 and normalized modal mass μ_1 of a PAM unit cell with a single mass. (a) Bandwidth BW for different combinations of f_1 and μ_1; (b) Optimal normalized modal mass $\mu_{1,\mathrm{opt}}$ to achieve optimal bandwidth at a given resonance frequency f_1; (c) Optimal bandwidth $\mathrm{BW}_{\mathrm{opt}}$ at a given resonance frequency f_1; (d) Normal incidence sound transmission loss for different f_1 and the corresponding $\mu_{1,\mathrm{opt}}$.

results are used to constrain the parameter space in the optimizations of the more complex PAM configurations.

The PAM resonance frequency f_1 is varied in the range 100 Hz to 1600 Hz and the normalized modal mass μ_1 from 3×10^{-3} to 20. The bandwidth BW resulting in this parameter range is shown in Figure 6(a). The results indicate that when f_1 is tuned to occur below or

Accepted Manuscript

within the frequency range in which BW is evaluated according to Equation 12, the resulting bandwidths are comparatively low. This can be explained by the STL dip which always occurs at f_1 and thus reduced the sound reduction performance of the PAM around this frequency. If, on the other hand, $f_1 > f_{\mathrm{max}}$, then much larger bandwidths can be achieved. In fact, for each fixed value of f_1 there is a unique μ_1 for which the bandwidth is maximal. This optimal normalized modal mass $\mu_{1,\mathrm{opt}}$ is plotted over f_1 in Figure 6(b). It can be seen that $\mu_{1,\mathrm{opt}}$ decreases for increasing values of f_1. The optimal bandwidth $\mathrm{BW}_{\mathrm{opt}}$ associated with different values of f_1 and the corresponding $\mu_{1,\mathrm{opt}}$ is shown in Figure 6(c). In general, higher bandwidths can be achieved when higher resonance frequencies are specified. However, if $f_1 \gg f_{\mathrm{max}}$, the optimal bandwidth converges to a maximum value $\mathrm{BW}_{\mathrm{max}}$ corresponding to the bandwidth in the limit $f_1 \to \infty$. This means that the bandwidth of a PAM with a single mass cannot be made arbitrarily large. For the given parameter setup, the maximum bandwidth is approximately $\mathrm{BW}_{\mathrm{max}} \approx 46.7\,\%$. The optimal bandwidth at $f_1 = 1600\,\mathrm{Hz}$ is $\mathrm{BW}_{\mathrm{opt}} = 45.3\,\%$ which is only $3\,\%$ below the maximum possible value. Thus, not much improvement of the bandwidth can be expected by further increasing the resonance frequency of the PAM.

The STL of the PAM with three different resonance frequencies 400 Hz, 800 Hz and 1600 Hz and the corresponding optimal normalized modal masses $\mu_{1,\mathrm{opt}}$ is shown in Figure 6(d). The STL spectra are shown for frequencies from 50 to 1600 Hz with the frequency ranged used for evaluating BW highlighted by the shaded region. In the case $f_1 = 400\,\mathrm{Hz}$ the optimal bandwidth is achieved with an anti-resonance at approximately 265 Hz. This results in STL values 6 dB over the mass-law in the frequency range between 230 and 290 Hz.

Accepted Manuscript

At 400 Hz the STL drops to nearly zero due to the PAM unit cell resonance at this frequency. When $f_1 = 800$ Hz, the optimal bandwidth is achieved with a higher anti-resonance frequency and it can be observed that at exactly $f_{\max} = 400$ Hz the STL of the PAM crosses the $\mathrm{TL}_{\mathrm{mass}} + 6$ dB curve. For $f_1 = 1600$ Hz the same point of intersection occurs, only the anti-resonance frequency is slightly lower such that the bandwidth of the PAM becomes slightly larger. This indicates that, at least for the present setup, the best bandwidth can be achieved when $f_1 > f_{\max}$ and the frequency range with the STL of the PAM greater than $\mathrm{TL}_{\mathrm{mass}} + 6$ dB is tuned such that the upper frequency of this band coincides with $f_{\max}$.

B. Optimization method

For the more complex PAM configurations with multiple masses or multiple PAM layers, the optimization problem can be formalized as follows:

$$
\begin{aligned}
\underset{\mathbf{p}_1,\ldots,\mathbf{p}_n}{\text{maximize}} \quad & \mathrm{BW}(\mathbf{p}_1,\ldots,\mathbf{p}_n) \\
\text{with} \quad & \mathbf{p}_j = (f_{1,j},\ldots,f_{m,j},\mu_{1,j},\ldots,\mu_{m,j})^T \\
\text{subject to} \quad & f_{i,j} \begin{cases} = 3 f_{\max} & \text{if} \quad i = 1 \\ \in [f_{\min}, f_{\max}] & \text{else} \end{cases} \\
& \mu_{i,j} \in [10^{-3}, 10^{2}]\,.
\end{aligned}
\tag{14}
$$

This means that the bandwidth BW should be maximized with respect to the design variables given in the vectors $\mathbf{p}_1$ to $\mathbf{p}_n$. Each vector $\mathbf{p}_j$ contains the eigenfrequencies $f_{1,j},\ldots,f_{m,j}$ and normalized modal masses $\mu_{1,j},\ldots,\mu_{m,j}$ of the j-th PAM layer. In order to keep the design variable space small, the eigenfrequencies and normalized modal masses are constrained as

Accepted Manuscript

follows: For each PAM layer, the first eigenfrequency $f_{1,j}$ is constrained to equal to three times $f_{\max}$. This constraint has been chosen based on the results in section III A where it was found that one PAM resonance frequency should be as large as possible. When $f_{1,j} = 3f_{\max}$, the bandwidth is already quite close to the maximum possible bandwidth value. Therefore, this value has been chosen as a reasonable value for $f_{1,j}$. All further eigenfrequencies $f_{2,j}, \ldots, f_{m,j}$ of each layer are constrained to appear between $f_{\min}$ and $f_{\max}$. This ensures that additional anti-resonances occur within this frequency range. The lower limit of the modal masses was chosen because for very small $\mu_{i,j}$ the change in BW is negligible. The upper limit was specified because for high values of $\mu_{i,j}$ the corresponding eigenmode of the PAM does hardly couple with the sound waves and therefore does not contribute to additional anti-resonances. For the optimization of stacked PAM, the total surface mass density is fixed at m_0'' by setting the static surface mass density of each layer to $m_{0,j}'' = m_0''/n$. The distance between each layer is fixed at $d_{j-1,j} = 5\,\mathrm{mm}$, because, as shown in Figure 4(b), for very small layer spacings the effect of $d_{j-1,j}$ on the STL of multi-layered PAM is negligible.

The optimization problem in Equation 14 is solved using the so-called particle swarm optimization algorithm (Kennedy and Eberhart, 1995). To increase the probability that the global optimum has been found, the optimization is repeated 20 times with different randomized initializations. The set of design variables leading to the highest bandwidth in these runs is then chosen as the optimal configuration.

Accepted Manuscript

C. Unit cell with multiple masses

First, it is investigated how the bandwidth of a PAM can be improved by changing the number of masses inside one unit cell. Increasing the number of masses as well as changing the shape and distribution of masses to introduce asymmetries corresponds to increasing the number of modes m to be considered in the optimization. Thus, m has been varied between 1 (i.e. only one mass per unit cell) and 4 to investigate the impact on the bandwidth. As shown in section II C 1, $m = 2$ could, for example, be realized using a unit cell with two equal semicircular masses. An asymmetric unit cell can be created by using two semicircular masses with different thicknesses (there are other possible ways to introduce asymmetries, for example by changing the mass diameter or general shape). Even though only two masses are used in this case, the asymmetry leads to an additional eigenmode with significant coupling with the incident sound field and thus m increasing to 3. In order to further increase the number of eigenmodes to $m = 4$, each of the semicircular masses with different thicknesses can be split up into two parts. This will generate a unit cell with four quartercircular masses, where two mass pairs have equal thickness, and $m = 4$. More details about how the modal parameters of a unit cell can be altered specifically using suitable mass arrangements can be found in the literature (e.g. (Chen *et al.*, 2014; Leblanc and Lavie, 2017; Lu *et al.*, 2020)).

The optimized modal parameters of the four different PAM unit cells are shown in Table III. The corresponding bandwidth and sound transmission loss values are shown in Figure 7(a) and Figure 7(b), respectively.

TABLE III. Optimized modal parameters of the optimized PAM unit cells with multiple masses.

	$m=1$		$m=2$		$m=3$		$m=4$	
i	f_i	μ_i	f_i	μ_i	f_i	μ_i	f_i	μ_i
1	1200	0.0858	1200	0.0826	1200	0.0803	1200	0.0759
2	—	—	306	42.8	320	40.5	353	41.5
3	—	—	—	—	271	60.1	299	43.8
4	—	—	—	—	—	—	262	53.8
	Hz	—	Hz	—	Hz	—	Hz	—

In the first case with only one mass per unit cell, the resonance frequency is $f_1 = 1200\,\mathrm{Hz}$, corresponding to the constraint defined in Equation 14, and the optimized μ_1 corresponds to the value of $\mu_{1,\mathrm{opt}}$ obtained in section III A. The resulting optimized bandwidth is BW = 44.2 %. As shown in Figure 7(a), the bandwidth can be increased to up to 56 % by increasing the number of modes of one unit cell to $m = 4$. The data in Table III shows for every additional mode a new resonance frequency with $\mu_i > 10$ appears within the frequency range of interest. This leads to new anti-resonances appearing in the STL spectrum with each additional mode. The TL results in Figure 7(b) indicate that the transmission loss then oscillates above the $\mathrm{TL}_{\mathrm{mass}} + 6\,\mathrm{dB}$ curve over a wider frequency range, thus leading to an increase of the bandwidth with each additional anti-resonance. However, all curves in Figure 7(b) have in common that they intersect the $\mathrm{TL}_{\mathrm{mass}} + 6\,\mathrm{dB}$ curve right at $f_{\max} =$

Accepted Manuscript

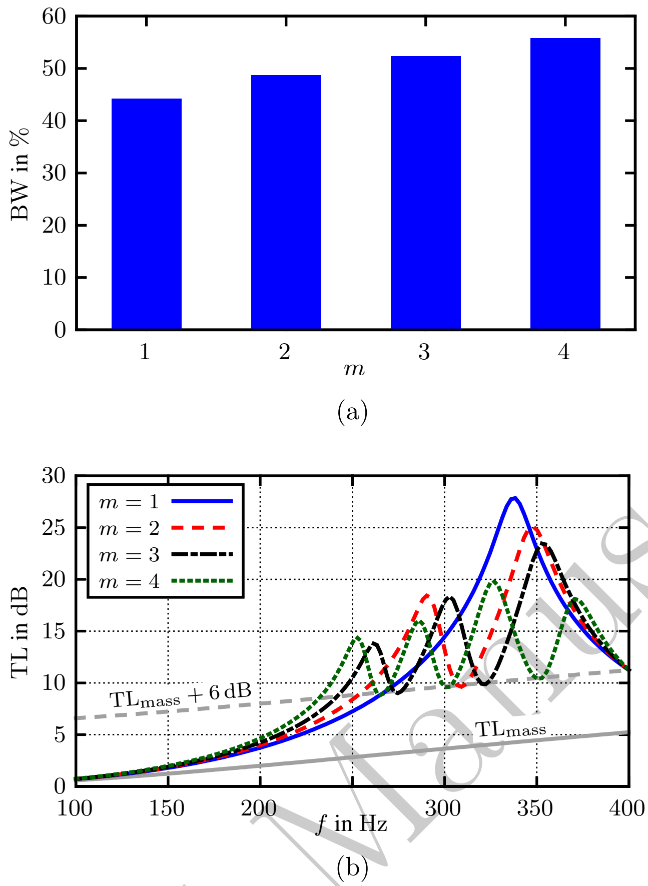

FIG. 7. (Color online) Bandwidth and transmission loss of the optimized PAM unit cells with multiple masses. (a) Bandwidth BW; (b) Normal incidence transmission loss TL.

400 Hz. This was already observed in the single mass case (see section III A) and therefore also seems optimal for PAM designs with multiple masses per unit cell.

D. Stacked PAM layers

Table IV lists the optimized modal parameters for multi-layered PAM configurations, each with only one mass per unit cell (i.e. $m = 1$), for different numbers of layers $n = 1$ to 4. The resulting optimized bandwidths are shown in Figure 8(a) and Figure 8(b) shows the

Accepted Manuscript

TABLE IV. Optimized modal parameters of the optimized multi-layered PAM configurations.

	$n = 1$		$n = 2$		$n = 3$		$n = 4$	
j	f_1	μ_1	f_1	μ_1	f_1	μ_1	f_1	μ_1
1	1200	0.0858	1200	0.0941	1200	0.0747	1200	0.0621
2	—	—	1200	0.0667	1200	0.0993	1200	0.102
3	—	—	—	—	1200	0.0557	1200	0.0483
4	—	—	—	—	—	—	1200	0.0795
	Hz	—	Hz	—	Hz	—	Hz	—

Accepted Manuscript

corresponding TL curves. In accordance with the optimization constraints, the resonance frequencies f_1 of each layer are equal to 1200 Hz. When more then one layer is considered, the normalized modal masses μ_1 of each layer are optimized to different values in order to achieve different anti-resonance frequencies for each layer that overlay in the resulting STL spectra.

It is noteworthy that using multiple PAM layers leads to very similar bandwidth improvements, as shown in Figure 8(a), compared to using a single PAM layer with multiple masses. In fact, the maximum bandwidth at $n = 4$ is 55.8 %, which is only slightly smaller than in Figure 7(a) for $m = 4$ (56 %). This indicates that, from the perspective of bandwidth improvement, it does not significantly matter if the bandwidth is improved by using one PAM with multiple masses, or stacking multiple PAM layers with a single mass, or a combination

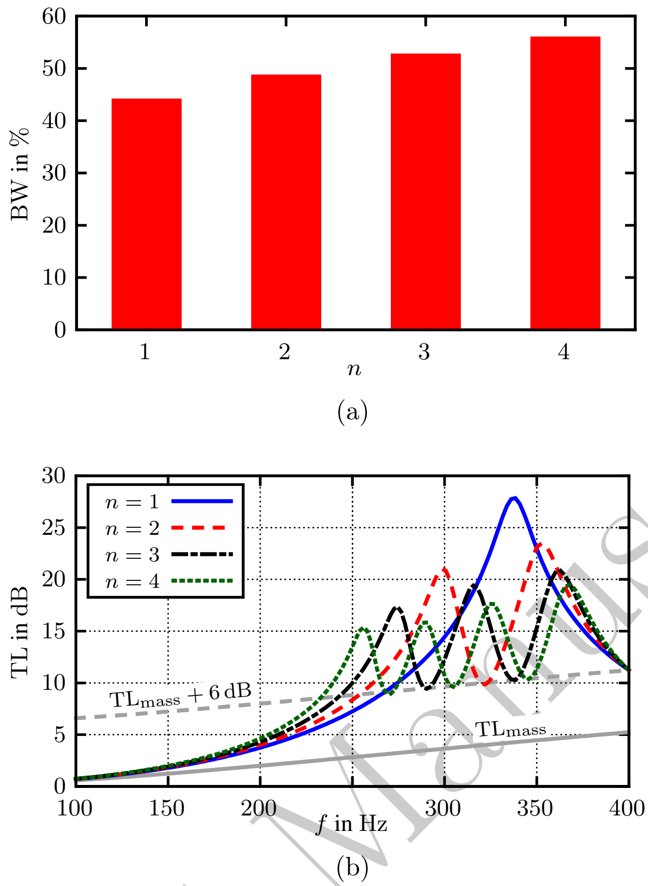

FIG. 8. (Color online) Bandwidth and transmission loss of the optimized multi-layered PAM configurations, each layer with a single mass per unit cell. (a) Bandwidth BW; (b) Normal incidence transmission loss TL.

thereof. This is also confirmed by the TL curves in Figure 8(b), which look very similar to the results in Figure 7(b), only with slightly different resonances and anti-resonances. The TL also oscillates above the $\mathrm{TL}_{\mathrm{mass}} + 6\,\mathrm{dB}$ line over a continuous frequency interval with increasing width for increasing number of layers. As in the multiple mass cases, all STL curves intersect the $\mathrm{TL}_{\mathrm{mass}} + 6\,\mathrm{dB}$ curve at the maximum frequency of interest. It should also be emphasized that, as in Figure 7(a), the peak STL values at the anti-resonances are reduced when more layers are added. The explanation for this is that, in order to keep the

Accepted Manuscript

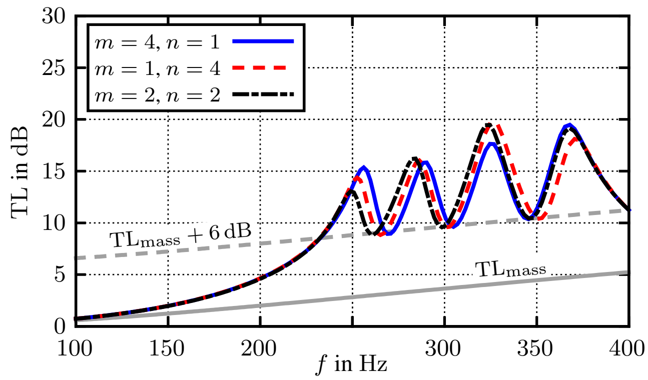

FIG. 9. (Color online) Normal incidence transmission loss TL of the optimized PAM configurations with $m \cdot n = 4$.

total surface mass density constant at $0.5\,\mathrm{kg\,m^{-2}}$, the static surface mass density of each layer is reduced. Very similar to the mass-law, this leads to a reduction of the maximum STL values of each layer, compared to the single layer case, by approximately $20\,\lg n$.

E. Combination of multi-mass and multi-layer PAM

The results shown in the previous sub-sections have shown that virtually the same bandwidths can be achieved either by using a single PAM with a certain number of modes m or by using $n = m$ layers of PAM, each with a single mass per unit cell. A reasonable question would be, if it is possible to further improve the bandwidths by using combinations of multiple PAM layers each with numbers of eigenmodes greater than one. Addressing this question, Figure 9 shows the optimized normal incidence transmission loss TL for three specific PAM configurations: The first configuration ($m = 4$, $n = 1$) corresponds to a single PAM layer with four eigenmodes (see Figure 7(b)). The second configuration ($m = 1$,

Accepted Manuscript

$n = 4$) is a four layer stack of PAM with a single mass per unit cell (see Figure 8(b)). Finally, the last configuration ($m = 2$, $n = 2$) represents an optimized two-layer PAM with two eigenmodes in each layer. Despite some small variations in the peaks and dips in the TL spectra shown in Figure 9, the overall bandwidth is virtually the same in all three cases. This indicates that the optimum bandwidth of a PAM structure is mainly governed by the total number of eigenmodes (in this case, where every layer has the same number of modes: $m \cdot n$). The impact of the specific distribution of the eigenmodes along multiple layers is small compared to this. Consequently, the number of layers and PAM eigenmodes can be quite readily adapted to specific noise control applications.

IV. CONCLUSIONS

In this contribution it was investigated if the bandwidth of plate-type acoustic metamaterials can be improved by using multiple masses in one unit cell or multiple layers of PAM stacked on top of each other. For this purpose, an efficient model for computing the sound transmission loss of single- and multi-layer PAM using the modal parameters of the PAM unit cells and the transfer matrix method was employed. This model was validated using FEM simulations and experimental data. It was then used in a particle swarm optimization algorithm to maximize the bandwidth between 100 and 400 Hz of different multi-mass and multi-layer PAM configurations. For all optimizations, the total surface mass density was the same to ensure comparability.

The optimization results have shown that in each case the bandwidth can be increased from 44.2 % to up to 56 % and 55.8 %, respectively. Furthermore, it could be shown that

Accepted Manuscript

the same bandwidth improvement can be achieved either by adding masses to a unit cell or adding more PAM layers. Thus, the design of PAM with improved bandwidth is flexible in this regard and can be adapted to non-acoustic constraints in practical noise control applications.

ACKNOWLEDGMENTS

This work has been performed under the framework of the German-Canadian joint research project New Acoustic Insulation Metamaterial Technology for Aerospace (NAIMMTA), funded by the Federal Ministry of Education and Research (grant number: 03INT504AB). The financial support is gratefully acknowledged by the authors.

Accepted Manuscript

Allard, J. F., and Atalla, N. (**2009**). *Propagation of Sound in Porous Media: Modelling Sound Absorbing Materials*, 2 ed. (John Wiley & Sons, Chichester), pp. 244–257.

Ang, L. Y. L., Koh, Y. K., and Lee, H. P. (**2018**). "Plate-type acoustic metamaterial with cavities coupled via an orifice for enhanced sound transmission loss," Appl. Phys. Lett. **112**(5), 051903, doi: 10.1063/1.5019602.

Bies, D. A., and Hansen, C. H. (**2009**). *Engineering Noise Control: Theory and Practice* (Spon Press, London), p. 368.

Chen, Y., Huang, G., Zhou, X., Hu, G., and Sun, C.-T. (**2014**). "Analytical coupled vibroacoustic modeling of membrane-type acoustic metamaterials: Plate model," J. Acoust. Soc. Am. **136**(6), 2926–2934, doi: 10.1121/1.4901706.

Fahy, F. J., and Gardonio, P. (**2007**). *Sound and structural vibration: radiation, transmission and response* (Academic press, Oxford), p. 298.

Huang, T.-Y., Shen, C., and Jing, Y. (**2016**). "Membrane- and plate-type acoustic metamaterials," J. Acoust. Soc. Am. **139**(6), 3240–3250, doi: 10.1121/1.4950751.

Kennedy, J., and Eberhart, R. (**1995**). "Particle swarm optimization," in *Proceedings of ICNN'95 - International Conference on Neural Networks*, Perth, Australia, pp. 1942–1948, doi: 10.1109/ICNN.1995.488968.

Kurtze, G. (**1959**). "Light-weight walls with high transmission loss," Acta Acust. united Ac. **9**(6), 441–445.

Langfeldt, F., and Gleine, W. (**2019**a). "Improved sound transmission loss of glass wool with acoustic metamaterials," in *Proceedings of the 26th International Congress on Sound and Vibration*, Montréal, Canada.

Langfeldt, F., and Gleine, W. (**2019**b). "Membrane- and plate-type acoustic metamaterials with elastic unit cell edges," J. Sound Vib. **453**, 65–86, doi: 10.1016/j.jsv.2019.04.018.

Langfeldt, F., and Gleine, W. (**2020**). "Impact of manufacturing inaccuracies on the acoustic performance of sound insulation packages with plate-like acoustic metamaterials," SAE Technical Paper 2020-01-1562, in press.

Langfeldt, F., Hoppen, H., and Gleine, W. (**2020**). "Broadband low-frequency sound transmission loss improvement of double walls with helmholtz resonators," J. Sound Vib. **476**, 115309, doi: 10.1016/j.jsv.2020.115309.

Langfeldt, F., Kemsies, H., Gleine, W., and von Estorff, O. (**2017**). "Perforated membrane-type acoustic metamaterials," Phys. Lett. A **381**(16), 1457–1462, doi: 10.1016/j.

Accepted Manuscript

physleta.2017.02.036.

Leblanc, A., and Lavie, A. (**2017**). "Three-dimensional-printed membrane-type acoustic metamaterial for low frequency sound attenuation," J. Acoust. Soc. Am. **141**(6), EL538–EL542, doi: 10.1121/1.4984623.

Lu, Z., Yu, X., Lau, S.-K., Khoo, B. C., and Cui, F. (**2020**). "Membrane-type acoustic metamaterial with eccentric masses for broadband sound isolation," Appl. Acoust. **157**, 107003, doi: 10.1016/j.apacoust.2019.107003.

Ma, G., and Sheng, P. (**2016**). "Acoustic metamaterials: From local resonances to broad horizons," Sci. Adv. **2**(2), doi: 10.1126/sciadv.1501595.

Mei, J., Ma, G., Yang, M., Yang, Z., Wen, W., and Sheng, P. (**2012**). "Dark acoustic metamaterials as super absorbers for low-frequency sound," Nat. Commun. **3**, doi: 10.1038/ncomms1758.

Yang, M., Ma, G., Wu, Y., Yang, Z., and Sheng, P. (**2014**). "Homogenization scheme for acoustic metamaterials," Phys. Rev. B **89**(6), doi: 10.1103/PhysRevB.89.064309.

Yang, Z., Dai, H. M., Chan, N. H., Ma, G. C., and Sheng, P. (**2010**). "Acoustic metamaterial panels for sound attenuation in the 50-1000 Hz regime," Appl. Phys. Lett. **96**(4), doi: 10.1063/1.3299007.

Zangeneh-Nejad, F., and Fleury, R. (**2019**). "Active times for acoustic metamaterials," Rev. Phys. **4**, 100031, doi: 10.1016/j.revip.2019.100031.